Available online at www.sciencedirect.com

SciVerse ScienceDirect

Ceramics International 39 (2013) 2343–2352

CERAMICS INTERNATIONAL

www.elsevier.com/locate/ceramint

ZnO nanorods surface-decorated by WO_3 nanoparticles for photocatalytic degradation of endocrine disruptors under a compact fluorescent lamp

Sze-Mun Lam, Jin-Chung Sin, Ahmad Zuhairi Abdullah, Abdul Rahman Mohamed*

School of Chemical Engineering, Universiti Sains Malaysia, Engineering Campus, 14300 Nibong Tebal, Pulau Pinang, Malaysia

Received 23 July 2012; received in revised form 28 August 2012; accepted 28 August 2012
Available online 4 September 2012

Abstract

Nanoscaled tungsten oxide (WO_3) particles coated on ZnO nanorods (ZNRs) were newly synthesized by combining a hydrothermal technique with a chemical solution process. The structure, morphologies and compositions of the as-prepared WO_3–ZNR nanocomposites were characterized through XRD, FESEM, TEM and Raman measurements. The results revealed that pure monoclinic WO_3 nanoparticles with an average size range of 18–26 nm were distributed on the surfaces of ZNRs and attached strongly. Particularly, the optical properties as well as photocatalytic characteristics of pure ZNRs and WO_3–ZNR nanocomposites with different loadings of WO_3 were also examined. The absorption of WO_3–ZNR nanocomposites was redshifted due to effective immobilization of WO_3 on ZNRs. Under irradiation of a 55 W compact fluorescence lamp, the photocatalytic activities of the WO_3–ZNR nanocomposites were superior to those of pure ZNRs and P25 in the degradation of resorcinol (ReOH). Furthermore, WO_3–ZNR nanocomposites showed very favorable recycle use potential and high sedimentation rate. Other endocrine disrupting chemicals (EDCs) such as phenol, bisphenol A (BPA) and methylparaben were also successfully photodegraded under identical conditions. These characteristics showed the practical applications of the WO_3–ZNR nanocomposites in indoor environmental remediation.

Keywords: B. Nanocomposite; Endocrine disrupting chemical; Hydrothermal; Photocatalysis

1. Introduction

Zinc oxide, a typical kind of II–IV compound semiconductor with a wide band gap (3.37 eV) has garnered much attention owing to its wide potential applications in luminescence, sensors, solar cells, surface acoustic wave filters and in gas and liquid phase pollution control [1,2]. In most of the catalytic applications, large surface area and critical pore size are required for interaction with active sites and diffusion of reactive species [3], this led to broad interest in the development of one-dimensional (1D) ZnO-based nanorods, nanowires and nanobelts. In the photocatalytic reaction, quick recombination of charge carriers resulting in a waste of energy provided by the photon can be regarded as one of main factors influencing efficiency of the photocatalytic process. Several researchers have proposed that the recombination effect can be significantly decreased in nanorod architecture compared to nanoparticles and should be favoured in photocatalytic applications [4,5]. Moreover, the large specific surface area and good dispersibility in solution rate have given ZnO nanorods a superior platform. ZnO nanorods are extensively utilized in the research of ultraviolet photodetectors, field effect transistors, light emitting device arrays and photocatalytic applications [6,7]. A suitable method to improve the photocatalytic ability of ZnO nanorods is post treatment of them, including coupling with semiconductors with narrower band gap to enhance the visible light responsiveness. Pure ZnO nanorods coupled with semiconductors such as Cu_2O, CdS, CdO and CeO_2 have been reported in literature [1,2,8,9]. In fact, coupling of ZnO 1D nanostructure such as a nanorod is a topic of huge interest for the last few years. To our knowledge, preparation of

*Corresponding author. Tel.: +60 45996410; fax: +60 45941013.
E-mail address: chrahman@eng.usm.my (A.R. Mohamed).

0272-8842/$ - see front matter © 2012 Elsevier Ltd and Techna Group S.r.l. All rights reserved.
http://dx.doi.org/10.1016/j.ceramint.2012.08.085

WO_3–ZnO nanorods by combining hydrothermal technique with a chemical solution process has not been reported.

ZnO-based nanorods can be prepared using different processes such as template-assisted growth, electrodeposition, chemical vapor deposition (CVD), thermal evaporation, hydrothermal method and so on [1,2,10,11]. Each preparation method has its own unique advantages and functional features. The hydrothermal process is of particular interest as nanorods can be formed in an ingenuous way at low temperatures and via simple chemical synthesis methods. In this paper, a facile and straightforward method has been utilized to synthesize the ZnO nanorods (ZNRs) decorated by dispersed WO_3 nanoparticles incorporating hydrothermal technique with a chemical solution method. The fabricated samples were characterized by different techniques and used for the photocatalytic degradation of various EDCs such as resorcinol (ReOH), phenol, bisphenol A (BPA) and methylparaben under a compact fluorescent light. The compact fluorescent lamp, which is utilized as household illumination, was chosen due to its efficient electricity, safety and long lifetime to light conversion. Thus, if the light intensity available from an ordinary compact fluorescent lamp would be adequate to degrade organic pollutants, it can offer a promising direction for the application of photocatalytic technology in indoor environments.

2. Experimental details

2.1. Preparation of WO_3–ZNRs

All the reagents used in this work were of analytical grade without further purification. The detailed synthesis procedure for pure ZNRs was as follows: 2.0 g of ZnO powder (Acros Organics, mean diameter 21 nm and surface area 5 $m^2 g^{-1}$) was weighed into a Teflon-lined stainless steel autoclave of 200 mL capacity. Subsequently, 150 mL of 30 vol% H_2O_2 solution was added in with stirring. The autoclave was sealed and maintained at a temperature of 180 °C for 24 h and then allowed to cool to room temperature naturally. The as-formed precipitates were filtered, washed with deionized water and ethanol and dried in air at 60 °C for 12 h. For the preparation of WO_3–ZNR nanocomposites, 1.0 g of ZNRs was dispersed in 50 mL deionized water and the suspension was ultrasonicated for 30 min. Then, a stoichiometric amount of ammonium metatungstate in 0.9 mL of NH_4OH (25 wt% NH_3) was added to the ZnO suspension and stirred magnetically for 12 h. The as-formed precipitates were filtrated, washed with deionized water and ethanol and dried in air at 60 °C for 12 h. Subsequently, the prepared samples were calcined at 400 °C for 2 h with a heating rate of 2 °C min^{-1}.

2.2. Characterizations

The crystal structures of the obtained samples were measured using an X-ray diffractometer (XRD; Philips PW1820) with Cu Kα radiation. The morphology of the nanocrystallites was studied using a field emission-scanning electron microscope (FESEM; LEO SUPRA 50 VP) and the microstructures were analyzed in-depth using a transmission electron microscope (TEM) along with a high resolution transmission electron microscope (HRTEM; Philips CM-12). The composition of WO_3 in ZNRs was verified using energy dispersive X-ray spectroscopy (EDX). Raman spectra of the WO_3-coupled samples were analyzed at room temperature using a Raman spectrometer (Reinashaw). The absorption spectra were obtained using a UV–vis spectrometer (Perkin Elmer; Lambda 35) with $BaSO_4$ as reference. The photoluminescence (PL) measurement was performed using a Spectrofluorometer (Perkin Elmer; Lambda S55) using a Xe lamp with an excitation wavelength of 325 nm at room temperature.

2.3. Photocatalytic experiment

The photocatalytic activities of the synthesized WO_3–ZNRs were evaluated by the degradation of a ReOH aqueous solution. The experiments were carried out as follows: 100 mg of the samples was dispersed in 100 mL of 1.8×10^{-4} M ReOH solution in a 150 mL beaker. During all experiments, air was bubbled through the solution at a fixed flow rate of 6 L min^{-1} using a specular draft tube. The suspension was continuously stirred with the aid of a magnetic stirrer. The heterogeneous mixture was equilibrated for 1 h in the dark. Subsequently, the solution was irradiated under a 55 W compact fluorescent lamp. The average light intensity striking the surface of the reaction solution was about 14500 lx, as measured by a digital luxmeter. This lamp was fixed about 12 cm above the reaction solution. At specific time intervals, 2 mL of the sample was withdrawn from the system, centrifuged and then the concentration of the ReOH at different time intervals was monitored by HPLC (Perkin Elmer Series 200). The HPLC unit consisted of isocratic pumps from Varian with a UV–vis detector. A *C*18 column (150 mm-length × 4.6 mm-ID × 5 μm particle size) was used in sample analysis at a flow rate of 1 mL min^{-1}. Experimental conditions for the liquid chromatography methods are shown in Table 1. To monitor the extent of mineralization during the ReOH degradation, changes in total organic carbon (TOC) were measured using a TOC analyzer (Shimadzu, TOC-V_{CPH}). By the same methods, the photocatalytic degradation efficiencies of other EDCs in the presence of prepared samples could be measured. In order to determine the reproducibility of the results, at least duplicated runs were carried out for each condition for averaging the results and the experimental error was found to be within ± 4%.

3. Results and discussion

3.1. Mechanism of nanorod formation

ZnO is a polar crystal showing positive and negative polar planes, rich in Zn and O. Typically, it was believed that the morphology of ZnO crystals was related to both

Table 1
Experimental conditions for the HPLC analysis.

Analyte	Mobile phase composition	Wavelength (nm)
ReOH	30% CH_3CN; 70% H_2O	238
Phenol	30% CH_3CN; 70% H_2O	254
BPA	80% CH_3CN; 20% H_2O	225
Methylparaben	50% CH_3OH; 50% H_2O	254

their intrinsic crystal structure and their external factors [12,13]. The possible mechanisms for the formation of single crystalline ZnO nanorod-like structures could be understood from the mechanism scheme given below.

$$ZnO + H_2O_2 \rightarrow ZnO_2 + H_2O \text{ (nucleation)} \quad (1)$$

In hydrothermal synthesis, the starting materials used were only ZnO powder and 30 vol% H_2O_2 aqueous solution and ZnO_2 was the sole resulting solid. Thus, it was believed that the formation of ZnO_2 may be formed as shown in Eq. (1). Since no valence change of Zn and O occurred, the formation of ZnO_2 was just through a precipitation conversion reaction [14]. That is, ZnO powder increasingly dissolved in the H_2O_2 aqueous solution under the relatively high temperature and high pressure hydrothermal environment, giving rise to Zn^{2+} ions. On the other hand, a part of H_2O_2 would dissociate in water to form peroxide anions (O_2^{2-}) according to Eq. (2).

$$H_2O_2 \leftrightarrow H^+ + HO_2^- \leftrightarrow 2H^+ + O_2^{2-} \quad (2)$$

When the concentration of Zn^{2+} and O_2^{2-} reached the saturation level, ZnO_2 nuclei were formed. It was considered that the as-prepared ZnO_2 nuclei may serve as building blocks for the formation of a single crystal growth of ZnO_2. With reaction time under proper heating conditions, the ZnO_2 nuclei concentration increased, which led to the growing of ZnO_2 nanocrystals into nanorod-like structures. Nevertheless, the as-prepared ZnO_2 nanorods were thermally unstable and would thoroughly decompose into ZnO and O_2 when heated in air at 400 °C for 2 h as in Eq. (3).

$$2ZnO_2 \rightarrow 2ZnO + O_2 \quad (3)$$

3.2. Characterization

Fig. 1 presents the XRD patterns of the pure ZNRs and the WO_3–ZNR nanocomposites with different loadings of WO_3. Fig. 1(a) shows that the crystal phases of the ZNRs agreed with hexagonal wurtzite structure (JCPDS no. 36-1451). From Fig. 1(b–d), all of the peaks can be indexed to the monoclinic phase of WO_3 except the diffraction peaks of ZnO, which was in good concordance with the standard data from JCPDS no. 072-1465. No peaks belonging to any other phase were identified, demonstrating the high purity of the products. As estimated from the

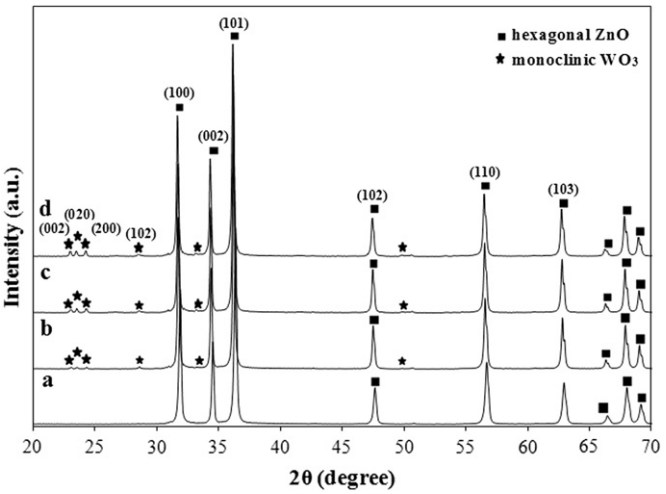

Fig. 1. X-ray diffraction patterns of (a) ZNRs, (b) WO_3(1 at%)–ZNRs, (c) WO_3(2 at%)–ZNRs and (d) WO_3(5 at%)–ZNRs.

half-peak width by Scherrer's equation, the average crystallite sizes of WO_3 were about 13.8, 23.6 and 40.3 nm accordingly for WO_3(1 at%)–ZNRs, WO_3(2 at%)–ZNRs and WO_3(5 at%)–ZNRs, respectively.

Fig. 2 depicts the typical field emission-scanning electron microscopy (FESEM) images of the pure ZNRs and WO_3–ZNR nanocomposites with different loadings of WO_3. As shown in Fig. 2(a), the pure ZNRs are composed of a number of non-uniform nanorod-like structures with an average diameter of about 79.5 nm. Fig. 2(b–d) revealed that all the samples had an average nanorod diameter of about 57.6 nm. The average diameter of the pure ZNRs was larger than all the WO_3–ZNR nanocomposites. The WO_3 compositions in the as-prepared samples were determined using the energy dispersive X-ray (EDX) analysis. The EDX results (inset of Fig. 2(b–d)) were collected from several spots of the decorated nanocomposite, which revealed them to be composed of zinc (Zn), oxygen (O) and tungsten (W) trace elements. The atomic ratios of W to ZnO increased from 0.012 ± 0.003 to 0.023 ± 0.005 and 0.068 ± 0.010 for WO_3(1 at%)–ZNRs, WO_3(2 at%)–ZNRs and WO_3(5 at%)–ZNRs, respectively. Elemental carbon (C) was also detected, which originated from the supporting carbon tape.

For detailed microstructure characteristics of the WO_3–ZNR nanocomposites, TEM along with HRTEM analyses were done and results are indicated in Fig. 3. Fig. 3(a) exhibits the typical TEM image of WO_3(2 at%)–ZNRs. It was clearly demonstrated that WO_3 particles in the range of 18–26 nm were attached to the surface of the ZNR matrix, which can coincide with the obtained XRD investigations. Fig. 3(b) shows the HRTEM image of the corresponding WO_3(2 at%)–ZNRs shown in Fig. 3(a). The WO_3 nanoparticles with irregular shapes can be observed on the surface of the ZNRs. In the case of the ZNRs, the space between the adjacent lattice fringes was 0.26 nm, corresponding to the interplanar distance of

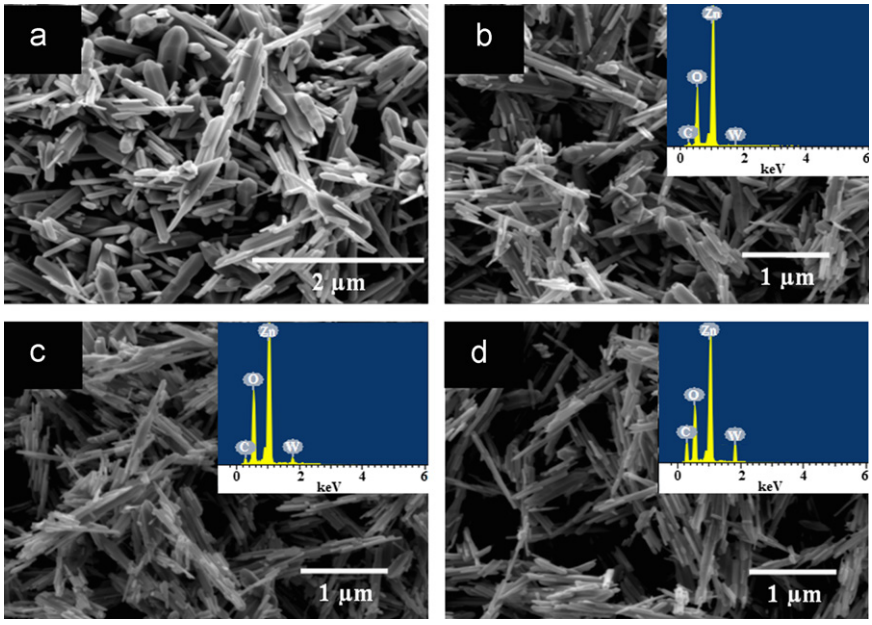

Fig. 2. FESEM images of samples (a) ZNRs, (b) WO_3(1 at%)–ZNRs, (c) WO_3(2 at%)–ZNRs and (d) WO_3(5 at%)–ZNRs. Inset part in figure is the EDX spectrum of the WO_3–ZNR nanocomposite.

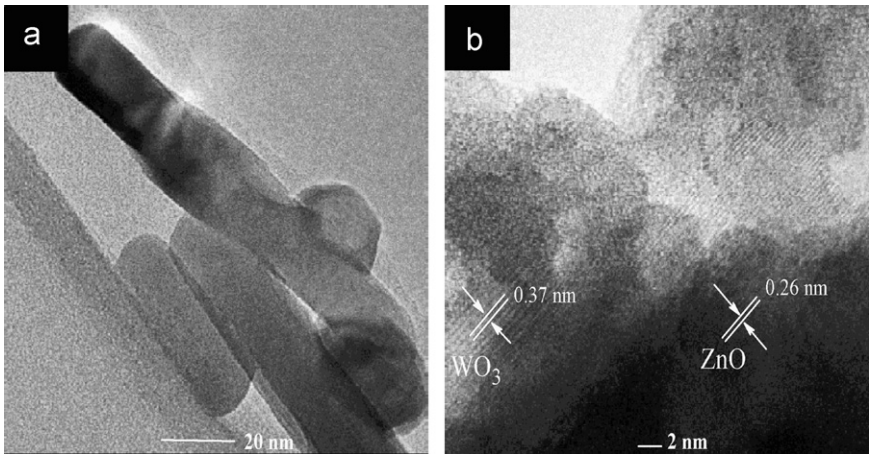

Fig. 3. TEM (a) and HRTEM images of WO_3(2 at%)–ZNR nanocomposites.

the (002) crystal fringes of wurtzite phase ZnO crystals, while the WO_3 nanoparticles were polycrystalline and the interplanar distance of 0.37 nm was in accordance with the (020) crystal fringe of monoclinic phase WO_3. From the TEM and HRTEM images, it can be verify that the WO_3–ZNR nanocomposites have highly crystalline structure, which was crucial for excellent photocatalytic materials.

Room temperature Raman spectra were also obtained to study the pure ZNRs and the three WO_3–ZNR nanocomposite samples as depicted in Fig. 4. The pure ZNR spectrum (Fig. 4(a)) was dominated by bands at 331, 380 and 438 cm^{-1}, which can be ascribed to the wurtzite ZnO [15]. Apart from distinctive bands of the ZnO wurtzite phase, from Fig. 4(b–d), Raman spectra of the decorating nanocomposite displayed dominant bands for WO_3 nanoparticles. Concretely, the bands at 280 and 313 cm^{-1} were assigned to the O–W–O bending modes of bridging oxygen and the peaks at 717 and 806 cm^{-1} were the corresponding stretching modes. Moreover, the intensity of the fundamental band of WO_3 increased with increasing WO_3 amount in the coupled semiconductors, which was in accordance with the earlier report [16]. As for ZnO bands, a slight increase in the intensities of the peaks can be observed with increasing WO_3 amounts in the nanocomposites. Nevertheless, the peak intensity ratios for the peak at 806 cm^{-1} of WO_3 to the peak at 438 cm^{-1} of ZnO increased with increasing WO_3 amount in the nanocomposites and they were 0.21, 0.84, and 2.91 for WO_3(1 at%)–ZNRs, WO_3(2 at%)–ZNRs and WO_3(5 at%)–ZNRs, respectively. The above results revealed that the resonant Raman effect

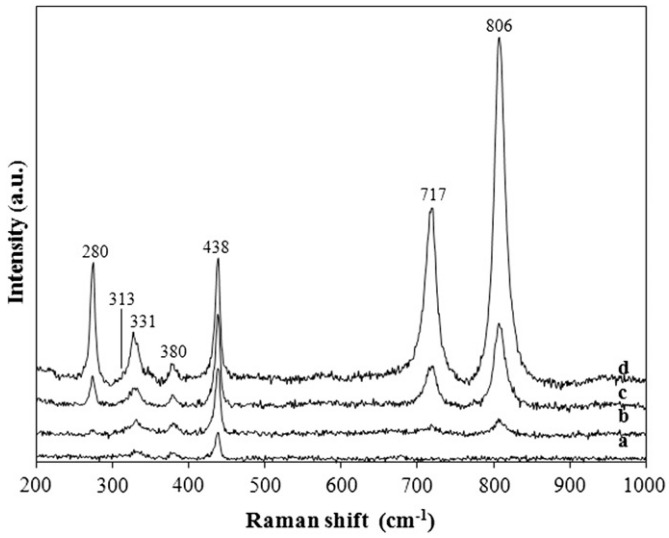

Fig. 4. Raman spectra for samples (a) ZNRs, (b) WO_3(1 at%)–ZNRs, (c) WO_3(2 at%)–ZNRs and (d) WO_3(5 at%)–ZNRs.

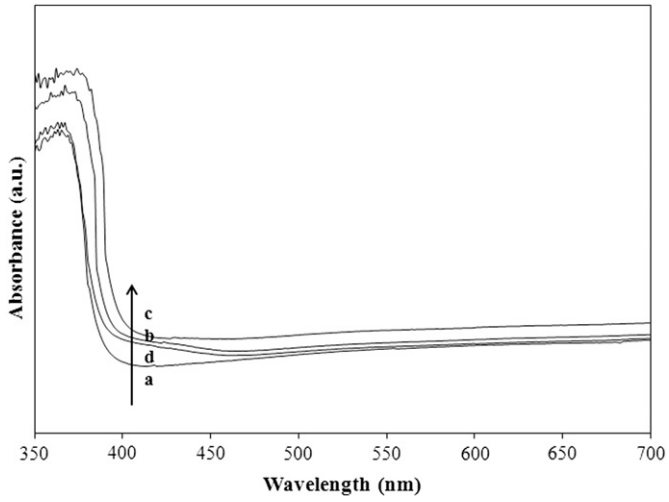

Fig. 5. UV–vis absorption spectra of (a) ZNRs and WO_3–ZNR nanocomposites with different WO_3 loadings (b) 1 at%, (c) 2 at% and (d) 5 at%.

for WO_3 became stronger relative to ZnO with an improvement of WO_3 amount in the WO_3–ZNR nanocomposites.

Fig. 5 shows the UV–vis absorption spectra of all the WO_3–ZNR nanocomposite samples along with the pure ZNRs. It can be observed that the band gap absorption at a wavelength of about 380–400 nm for the pure ZNRs and WO_3–ZNR nanocomposite samples. Comparing with pure ZNRs (Fig. 5(a)), additional broad tails from approximately 400–700 nm appeared in the spectra of the WO_3–ZNR nanocomposites (as recorded in Fig. 5(b–d)). The result indicated that the absorption of WO_3–ZNR nanocomposites was enlarged to the visible spectrum due to the existence of WO_3 that modified the optical band gap absorption. In addition, the absorption intensities of WO_3–ZNR nanocomposites increased and then decreased with increased loading of WO_3; the absorption intensity of WO_3(2 at%)–ZNRs was the highest. The band gap energies were calculated according to Eq. (4) [17]:

$$E_g = hc/\lambda = 1243.1/\lambda \quad (4)$$

where E_g is the band gap energy (eV), h is the Planck's constant (4.135667×10^{-15} eVs), c is the velocity of light (3×10^8 m/s), and λ is the wavelength (nm) of absorption onset. Using Eq. (4), the band gap energies of WO_3 (1 at%)–ZNRs, WO_3(2 at%)–ZNRs and WO_3(5 at%)–ZNRs were calculated as 3.17, 3.14 and 3.20 eV, respectively, lower than that of pure ZNRs (3.24 eV). All the WO_3–ZNR nanocomposite band gap absorptions showed a slight redshift when compared to pure ZNRs. This observation might be ascribed to the increase of particle size of WO_3 nanoparticles [18]. The above results revealed that the WO_3–ZNR nanocomposites can absorb in both UV and visible regions of the solar light. Hence, the absorption property deduced that the WO_3–ZNR nanocomposites could be promising in visible-light photocatalysis.

Photoluminescence (PL) spectra have been commonly utilized to evaluate the efficiency of charge carriers trapping, migration and transfer and to provide insight into the fate of electron–hole pairs in semiconductors [18]. Fig. 6 demonstrated that pure ZNRs and WO_3–ZNR nanocomposite samples exhibited the PL spectra peaks. In this study, the PL spectra of all samples were measured in the wavelength range of 350–700 nm. It can be observed that the pure ZNRs exhibited high intensity of PL signal (Fig. 6(a)). That was to say, the PL bands of ZNRs at the long wavelength range might be originated from oxygen vacancies [19]. PL spectra patterns of all the samples of WO_3–ZNR nanocomposites shown in Fig. 6(b–d) indicate the remarkable decrease in emission yield as compared to pure ZNRs. Such a decrease in

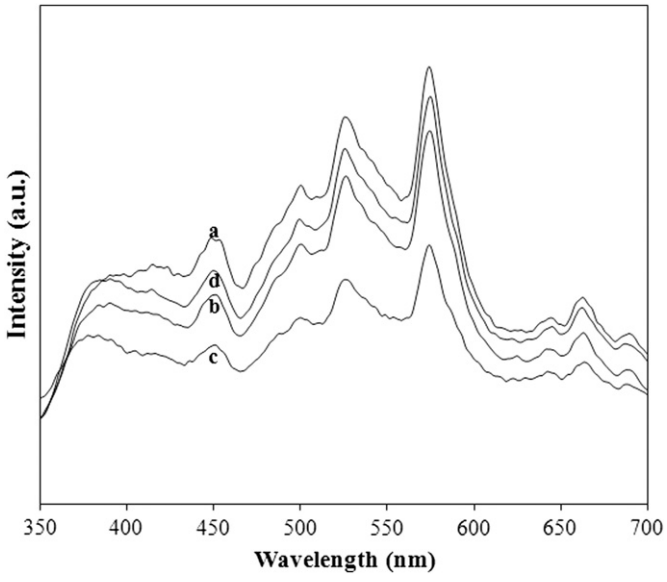

Fig. 6. Photoluminescence spectra of (a) ZNRs, (b) WO_3(1 at%)–ZNRs, (c) WO_3(2 at%)–ZNRs and (d) WO_3(5 at%)–ZNRs.

emission might be attributed to the efficient charge injection process between the ZNRs and WO_3 nanoparticles. Moreover, the PL intensity of WO_3–ZNR nanocomposites changed with the altering of the WO_3 amount. As for WO_3(2 at%)–ZNR nanocomposites, the PL spectrum pattern as shown in Fig. 6(c) was the lowest. Since the PL signal was the result of the recombination of charge carriers, the lower PL intensity indicated a lower recombination rate of charge carriers [11,20]. Thus, it might be hypothesized that WO_3(2 at%)–ZNRs should show higher photocatalytic activities than others.

3.3. Photocatalytic activities

The photocatalytic activities of the WO_3–ZNR nanocomposites were evaluated by the degradation of model substrate ReOH. ReOH is one of the endocrine disrupting chemicals (EDC) which are widely used in the manufacture of adhesives, tanneries, food processing, pharmaceuticals, etc. The exposure to ReOH can occur at its production sites, in effluent streams through its use in pharmaceutical applications and in cigarettes [21]. Evidence of the ReOH effect came from investigations of in vivo tests on rats and epidemiological studies of humans, where it may interfere with triiodothyronine (T3) and thyroxine (T4) metabolism, causing disruptions to thyroid activity [22]. The photocatalysis of this EDC in the presence of ZnO photocatalyst has not been greatly explored. Thus, ReOH was chosen as the model substrate to evaluate the photocatalytic activity of the products in this work. The HPLC profiles of an ReOH aqueous solution in the presence of WO_3(2 at%)–ZNR nanocomposites under irradiation by a 55 W compact fluorescent lamp at various durations are shown in Fig. 7(a). The ReOH showed a characteristic peak at retention time (RT) 2.60 min; it became weaker with extended irradiation time and nearly disappeared after 180 min. In addition to the above-mentioned main compound, the peak at RT 1.07 min could be assigned to muconic acid and the peak at RT 1.55 min could be attributed to pyrogallol intermediates when compared with the standard chemicals. This identification was also consistent with that reported in other studies [23]. Fig. 7(b) presents that the degradation efficiency reached 99.4% in 180 min. Under identical conditions of exposure to the compact fluorescent lamp, the WO_3–ZNR nanocomposite also showed much higher activities than pure ZnO (70.0% degradation efficiency) and P25 TiO_2 (63.3% degradation efficiency). Furthermore, the degradation of ReOH hardly occurred when the ReOH solution without the WO_3–ZNR nanocomposite was irradiated or when the solution with the nanocomposite was kept in the dark. In order to examine the effect of WO_3–ZNR nanocomposites on the mineralization of ReOH, the total organic carbon (TOC) value (Fig. 7(c)) of irradiated solution was also studied under irradiation of a 55 W compact fluorescence lamp. The initial TOC value before irradiation was

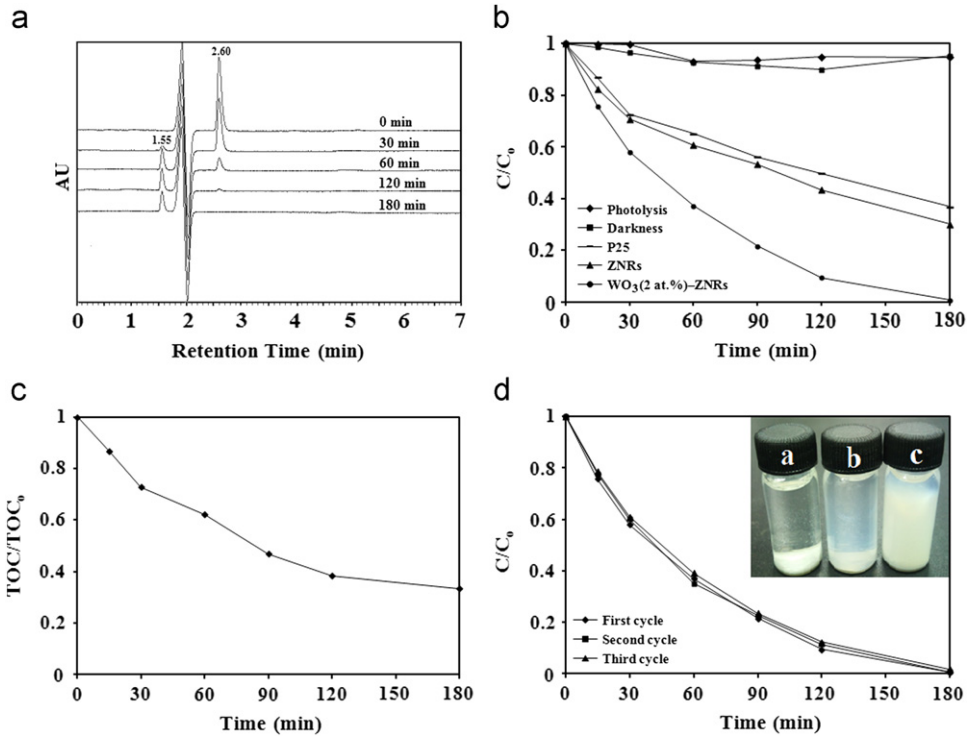

Fig. 7. Photocatalytic performance of WO_3(2 at%)–ZNRs in the degradation of ReOH. The suspensions were irradiated by a 55 W compact fluorescent lamp. (a) HPLC profiles of ReOH solution with WO_3–ZNRs at different time intervals, (b) ReOH concentration dependence on irradiation time using various photocatalysts, (c) changes of TOC during the photodegradation of ReOH, and (d) catalyst recycling in the degradation of ReOH. The inset shows the sedimentation for 2 h in aqueous suspensions of (a) WO_3(2 at%)–ZNRs, (b) ZNR and (c) P25 (dose of catalyst: 100 mg, ultrasonic treatment for 15 min).

16.9 mg L^{-1} and then the value steadily decreased during irradiation in 180 min. This verified the progressive mineralization of ReOH resulting from an effective decomposition of aromatic intermediates. The maximum TOC removal of ReOH was 66.7% at the point that the solution was almost completely degraded, which disclosed that other non-mineralized organic carbons still existed in the irradiated solution.

The reusability and separation ability of catalysts are very vital issues for practical applications. The WO_3 (2 at%)–ZNR nanocomposite could be readily recycled by simple filtration and washing after the reaction. As shown in Fig. 7(d), after a three-time recycling of WO_3–ZNR nanocomposites, there was still considerable degradation of ReOH in the aqueous solution. In fact, one of the advantages of WO_3–ZNR nanocomposites was that they can be conveniently separated to recycle the catalysts. According to the inset of Fig. 7(d), the pure ZNRs and WO_3–ZNR nanocomposites were sedimented from an aqueous suspension in 2 h, while the aqueous suspension of P25 was still relatively turbid.

Photocatalytic activities of the WO_3–ZNR nanocomposites with different loadings of WO_3 were confirmed by evaluating the degradation of ReOH in aqueous solution. As seen in Fig. 8(a), all the samples of WO_3–ZNR nanocomposites displayed enhanced photocatalytic activities compared to the pure ZNRs, which may be attributed to the cooperative roles between WO_3 nanoparticles and ZNRs. Particularly, WO_3(2 at%)–ZNRs exhibited the best performance on the photodegradation of ReOH among the four samples. The enhanced photocatalytic activity of WO_3–ZNR nanocomposites can be explained by the fact that the improvement in charge transmission between the semiconductors ZnO (wide band gap) and WO_3 (narrow band gap) prolonged the charge carriers lifetime. Additionally, the photocatalytic performance of the coupled semiconductors was also related to the surface contact between particles, geometry of the particles and particle size. At low WO_3(1 at%) amount, the effect of charge separation induced by WO_3 was not obvious because of the insufficiency of WO_3. Nevertheless, with increasing WO_3 amount to 5 at%, quite a number of WO_3 nanoparticles would surround some active sites of ZNRs and hinder the contact between nanorods and oxygen containing species, which resulted in the decrease of photocatalytic properties [24]. Hence, the WO_3(2 at%)–ZNRs with good dispersion and critical amount of WO_3 on the surface of ZNRs exhibited the highest photodegradation efficiency for ReOH.

The simple mechanistic illustrating the principle of charge separation for WO_3–ZNR nanocomposites shown in Scheme 1 was suggested. When WO_3 and ZNR form a coupled photocatalyst, WO_3 can be excited by photons under visible-light irradiation and ZNRs may remain unexcited. Upon fluorescent-light excitation, electrons from the ZNR and WO_3 would be promoted from the valence band to the conduction band, leaving behind holes in the valence band. As the conduction band of WO_3 was lower than that of ZNR, the photogenerated electrons of the ZNR conduction band will migrate to the conduction band of WO_3. Since the holes moved in the opposite direction from the electrons, photogenerated holes will be captured within the ZNR, causing the charge separation to become more effective [18,25]. The positive holes in the valence band can react with either OH^- or H_2O species adsorbed on the catalyst surface, producing highly reactive •OH radicals in aqueous solution. The electrons accumulated on the surface of WO_3 can rapidly transfer to O_2 to form the superoxide radical anion ($O_2•^-$). The $O_2•^-$ radicals can then react with H_2O to produce hydrogen peroxide (H_2O_2) and OH^- ions. Cleavage of H_2O_2 by the electrons further produced •OH radicals, which were responsible for the photodegradation of ReOH. Therefore, the difference in energy level between the coupled semiconductors in the WO_3–ZNR nanocomposites played the significant role in facilitating the efficient electron–hole separation along with broadening ZnO in visible light responsiveness.

The dose of WO_3(2 at%)–ZNR nanocomposites would also influence the numbers of the photogenerated electrons and holes and further influence the photodegradation efficiency when other experimental conditions remained

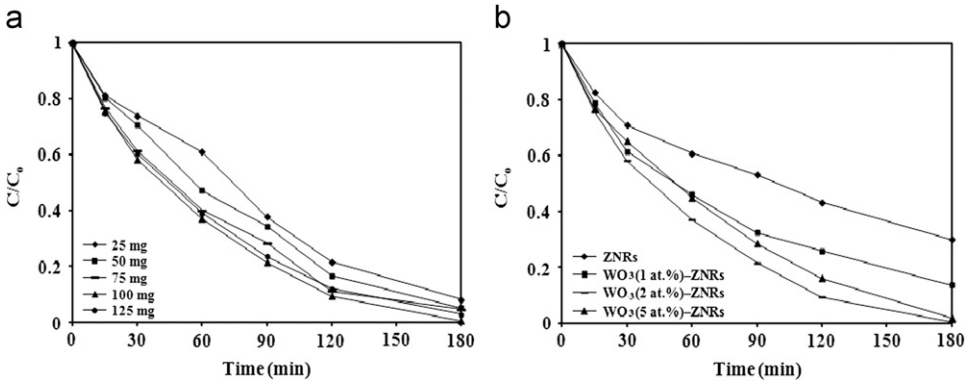

Fig. 8. Kinetics of photodegradation of 1.8×10^{-4} M ReOH with different (a) WO_3 loadings and (b) doses of WO_3(2 at%)–ZNRs under fluorescent-light (dose of catalyst: 100 mg; volume of ReOH: 100 mL).

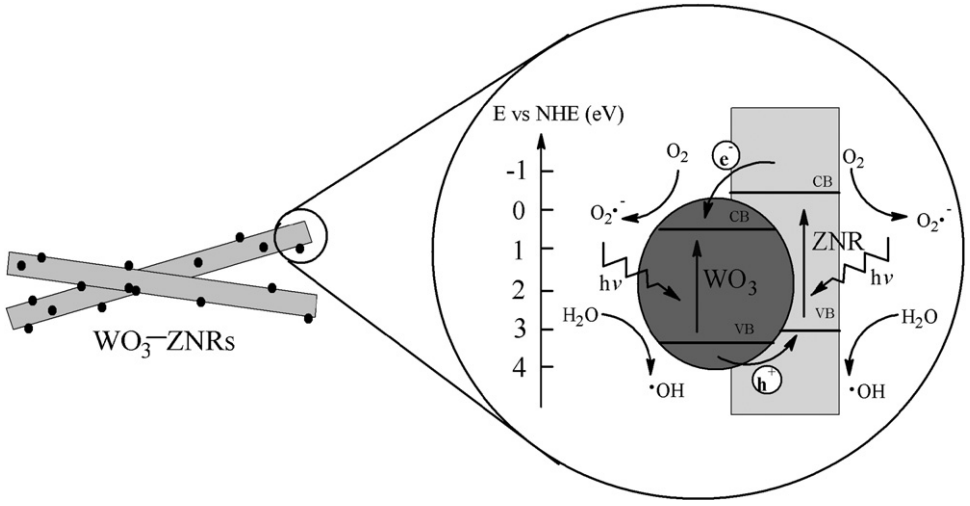

Scheme 1. Electron–hole separation and energy band structure of WO_3–ZNR nanocomposites under fluorescent-light irradiation.

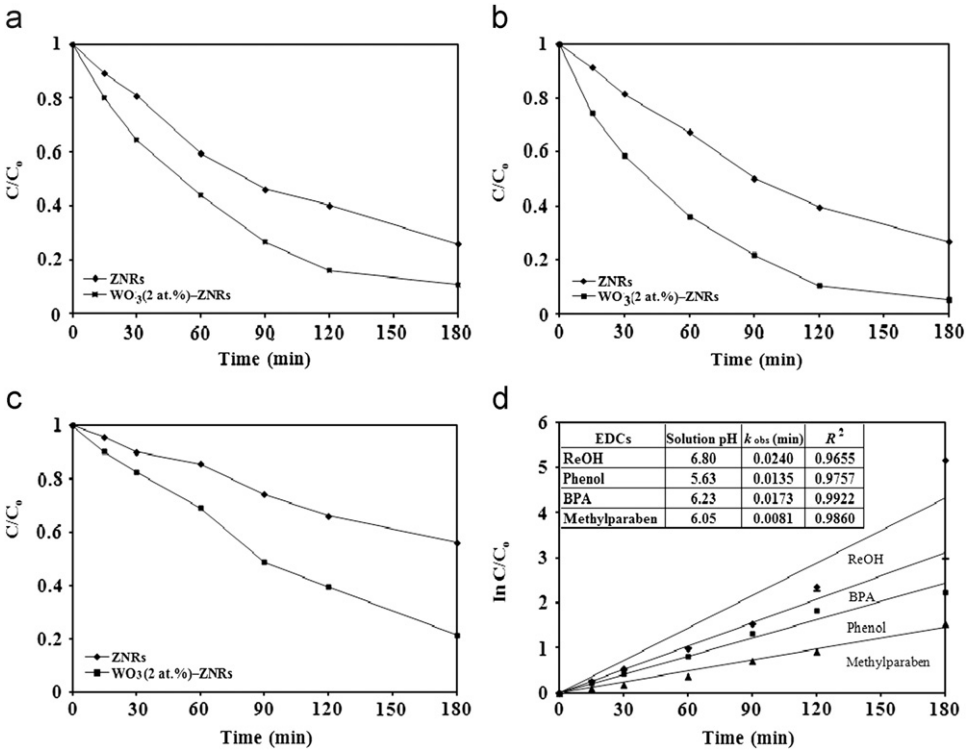

EDCs	Solution pH	k_{obs} (min)	R^2
ReOH	6.80	0.0240	0.9655
Phenol	5.63	0.0135	0.9757
BPA	6.23	0.0173	0.9922
Methylparaben	6.05	0.0081	0.9860

Fig. 9. Kinetics of photodegradation of (a) phenol, (b) BPA, (c) methylparaben under irradiation by a 55 W compact fluorescent lamp and (d) pseudo-first-order kinetics in photodegradation of various EDCs. The inset table shows the corresponding pH solution, observed rate constants and the linear fit (R^2) (dose of catalyst: 100 mg; volume of EDC: 100 mL; concentration of phenol: 2.1×10^{-4} M; concentration of BPA: 8.8×10^{-5} M; concentration of methylparaben: 1.3×10^{-4} M).

constant. Fig. 8(b) shows the kinetics of degradation with different doses of WO_3–ZNR nanocomposites. The photodegradation rates increased with the increase of quantity of WO_3–ZNR nanocomposites in the range of 25–100 mg due to the gradually increased active sites on the catalyst surface. When more than 100 mg WO_3–ZNR nanocomposites is used, there should be more electrons produced. Nevertheless, owing to the formation of a milky solution, a negative effect by reducing the transmittivity of light occurred. Moreover, the number of active sites on the catalyst surface was limited due to the loss in surface area occasioned by agglomeration at high catalyst dose [26]. Shrinking of the photoactivated volume of the suspension resulted in a reduced performance.

In addition to degradation of ReOH, the WO_3(2 at%)–ZNR nanocomposites could be used in photocatalytic degradation of other EDCs such as phenol, BPA and methylparaben as shown in Figs. 9(a–c). Like ReOH, these

EDCs are resistant to biodegradation and charcoal adsorption and may undergo natural reductive anaerobic degradation to yield potentially carcinogenic aromatic intermediates [27,28]. As seen in Fig. 9(a and b), phenol and BPA were efficiently degraded under identical experimental conditions as those in the degradation of ReOH. Methylparaben was degraded slowly in the presence of pure ZNRs under a compact fluorescent lamp and near 44.0% molecules were degraded in 180 min. When WO_3–ZNR nanocomposites were utilized, the photodegradation efficiency was improved to 78.6%. Obviously, WO_3–ZNR nanocomposites exhibited different activities in the photodegradation of different EDCs but they could improve the degradations of all EDCs stated above due to the catalytic ability. The photodegradation reactions of all EDCs obeyed a pseudo-first-order kinetic model with respect to the irradiation time. The results were nearly consistent with the linear equation [29]

$$\ln \frac{C_o}{C} = -k_{obs} t \quad (5)$$

where C_o is the equilibrium molar concentration of EDC (M) after 1 h dark adsorption, C is the concentration of EDC remaining in the solution at irradiation time of t (min), and k_{obs} is the observed first-order rate constant (min^{-1}). The variations in $\ln(C_o/C)$ as a function of irradiation time are given in Fig. 9(d). The linear relationship was achieved with more than 96% linear fit (R^2) as shown in the inset of Fig. 9(d), inferring an excellent concurrence with the given model.

4. Conclusions

In summary, WO_3–ZNR nanocomposites with different loadings of WO_3 have been obtained by combining the hydrothermal technique with a chemical solution method. The obtained WO_3–ZNR nanocomposites were verified by different methods including XRD, FESEM, TEM, Raman, UV–vis absorption and PL measurements. These nanocomposites could be used in fluorescent-light photodegradation of various EDCs including ReOH, phenol, BPA and methylparaben. They showed photocatalytic activities higher than pure ZNRs and P25 due to the cooperative roles between WO_3 and ZNRs which enhanced the separation of photogenerated charge carriers and surface properties of catalysts. Furthermore, the WO_3–ZNR nanocomposites were easy to recycle for photocatalytic purpose in that their activity remained almost constant after a three-time recycling. The synthesized WO_3–ZNR nanocomposites with properties of higher photocatalytic activity under a compact fluorescent lamp and easier separation for recycle use could be applied practically in an indoor environment when decomposing various pollutants.

Acknowledgments

This research was supported by a Research Universiti (RU) (Grant no. 854001) from Universiti Sains Malaysia and My PhD scholarship through Malaysia Government.

References

[1] R. Saravanan, H. Shankar, T. Prakash, V. Narayanan, A. Stephen, ZnO/CdO composite nanorods for photocatalytic degradation of methylene blue under visible light, Materials Chemistry and Physics 125 (2011) 277–280.
[2] Y. Wang, G.W. She, H.T. Xu, Y.Y. Liu, L.X. Mu, W.S. Shi, Cu_2O nanoparticles sensitized ZnO nanorod arrays: electrochemical synthesis and photocatalytic properties, Materials Letters 67 (2012) 110–11.
[3] C.C. Tsai, H. Teng, Regulation of the physical characteristics of titania nanotube aggregates synthesized from hydrothermal treatment, Chemistry of Materials 16 (2004) 4352–4358.
[4] Y.X. Wang, X.Y. Li, G. Lu, G.H. Chen, Y.Y. Chen, Synthesis and photo-catalytic degradation property of nanostructured-ZnO with different morphology, Materials Letters 62 (2008) 2359–2362.
[5] M.S. Mohajerani, A. Lak, A. Simchi, Effect of morphology on the solar photocatalytic behavior of ZnO nanostructures, Journal of Alloys and Compounds 485 (2009) 616–620.
[6] J.Y. Yang, Y. Lin, Y.M. Meng, Y.H. Liu, A two-step route to synthesize highly oriented ZnO nanotube arrays, Ceramics International 38 (2012) 4555–4559.
[7] W.I. Park, D.W. Kim, S.W. Jung, G.C. Yi, Catalyst-free growth of ZnO nanorods and their nanodevice applications, International Journal of Nanotechnology 3 (2006) 373–395.
[8] J. Nayak, S.N. Sahu, J. Kasuya, S. Nozaki, CdS–ZnO composite nanorods: synthesis, characterization and application for application degradation of 3,4-dihydroxy benzoic acid, Applied Surface Science (2008) 7215–7218.
[9] G.K. Lau, T.S. Zhang, G.K.L. Goh, Photochemical properties of CeO_2-coated ZnO nanorods, Journal of Nanoscience and Nanotechnology 10 (2010) 4733–4737.
[10] X. Liu, X.H. Wu, H. Cao, R.P.H. Chang, Growth mechanism and properties of ZnO nanorods synthesized by plasma-enhanced chemical vapor deposition, Journal of Applied Physics 95 (2004) 3141–3148.
[11] H.R. Pant, C.H. Park, B. Pant, L.D.T. Jing, H.Y. Kim, C.S. Kim, Synthesis, characterization, and photocatalytic properties of ZnO nanoflower containing TiO_2 NPs, Ceramics International 38 (2011) 2943–2950.
[12] J. Zhang, L.D. Sun, C.S. Liao, C.H. Yang, A simple route towards tubular ZnO, Chemical Communications 3 (2012) 262–263.
[13] P. Tonto, O. Mekasuwandumrong, S. Phatanasri, V. Pavarajarn, P. Praserthdam, Preparation of ZnO nanorod by solvothermal reaction of zinc acetate in various alcohols, Ceramics International 34 (2008) 57–62.
[14] S.Z. Liu, Y.C. Zhang, T.X. Wang, F.X. Yang, Green synthesis of hollow-nanostructured ZnO_2 and ZnO, Materials Letters 71 (2012) 154–156.
[15] J. Zhao, L. Wang, X.Q. Yan, Y. Yang, Y. Lei, J. Zhou, et al., Structure and photocatalytic activity of Ni-doped ZnO nanorods, Materials Research Bulletin 46 (2011) 1207–1210.
[16] M.A., Saepurahman, F.K., Abdullah Chong, Preparation and characterization of tungsten-loaded titanium dioxide photocatalyst for enhanced dye degradation, Journal of Hazardous Materials 176 (2010) 451–458.
[17] J. He, Q.Z. Cai, D. Zhu, Q. Luo, D.Q. Zhang, X.W. Li, et al., In-situ preparation of WO_3/TiO_2 composite film with increased photo quantum efficiency on titanium substrate, Current Applications in Physics 11 (2011) 98–100.
[18] J. He, Q. Luo, Q.Z. Cai, X.W. Li, D.Q. Zhang, Microstructure and photocatalytic properties of WO_3/TiO_2 composite films by plasma electrolytic oxidation, Materials Chemistry and Physics 129 (2011) 242–248.
[19] T.K. Jia, W.M. Wang, F. Long, Z.Y. Fu, H. Wang, Q.J. Zhang, Fabrication, characterization and photocatalytic activity of La-doped ZnO nanowires, Journal of Alloys and Compounds 484 (2009) 410–415.
[20] C.L. Yu, K. Yang, Q. Shu, J.C. Yu, F.F. Cao, X. Li, Preparation of WO_3/ZnO composite photocatalyst and its photocatalytic performance, Chinese Journal of Catalysis 32 (2011) 555–565.

[21] S.W. Lam, K. Chiang, T.M. Lim, R. Amal, G.K.C. Low, The effect of platinum and silver deposits in the photocatalytic oxidation of resorcinol, Applied Catalysis B: Environmental 72 (2007) 363–372.
[22] S.W. Lam, K. Chiang, T.M. Lim, R. Amal, G.K.C. Low, Effect of charge trapping species of cupric ions on the photocatalytic oxidation of resorcinol, Applied Catalysis B: Environmental 55 (2005) 123–132.
[23] A.B. Patil, K.R. Patil, S.K. Pardeshi, Ecofriendly synthesis and solar photocatalytic activity of S-doped ZnO, Journal of Hazardous Materials 183 (2010) 315–323.
[24] L.S. Wang, M.W. Xiao, X.J. Huang, Y.D. Wu, Synthesis, characterization, and photocatalytic activities of titanate nanotubes surface-decorated by zinc oxide nanoparticles, Journal of Hazardous Materials 161 (2009) 49–54.
[25] S.M. Lam, J.C. Sin, A.Z. Abdullah, A.R. Mohamed, Degradation of wastewaters containing organic dyes photocatalysed by zinc oxide: a review, Desalin, Water Treatment 41 (2012) 131–169.
[26] S.M. Lam, J.C. Sin, A.R. Mohamed, Parameter effect on photocatalytic degradation of phenol using TiO_2–P25/activated carbon (AC), Korean Journal of Chemical Engineering 27 (2010) 1109–1116.
[27] W.T. Tsai, M.K. Lee, T.Y. Su, Y.M. Chang, Photodegradation of bisphenol-A in a batch TiO_2 suspension reactor, Journal of Hazardous Materials 168 (2009) 269–275.
[28] J.C. Sin, S.M. Lam, A.R. Mohamed, K.T. Lee, Degrading endocrine disrupting chemicals from wastewater by TiO_2 photocatalysis: a review, International Journal of Photoenergy 2012 (2012) 1–23.
[29] D.Y. Fu, G.Y. Han, C.F. Meng, Size-controlled synthesis and photocatalytic degradation properties of nano-sized ZnO nanorods, Materials Letters 72 (2012) 53–56.